Slippage and viscosity predictions in carbon micropores and their influence on CO2 and CH4 transport

Mahnaz Firouzi and Jennifer Wilcox

Citation: J. Chem. Phys. **138**, 064705 (2013); doi: 10.1063/1.4790658
View online: http://dx.doi.org/10.1063/1.4790658
View Table of Contents: http://jcp.aip.org/resource/1/JCPSA6/v138/i6
Published by the American Institute of Physics.

Slippage and viscosity predictions in carbon micropores and their influence on CO_2 and CH_4 transport

Mahnaz Firouzi and Jennifer Wilcox[a)]
Department of Energy Resources Engineering, Stanford University, Stanford, California 94305-2220, USA

(Received 21 November 2012; accepted 16 January 2013; published online 14 February 2013)

Non-equilibrium molecular dynamics simulations of pure carbon dioxide and methane and their equimolar mixtures have been carried out with an external driving force imposed on carbon slit pores to investigate gas slippage and Klinkenberg effects. Simulations were conducted to determine the effect of pore size and exposure to an external potential on the velocity profile and slip-stick boundary conditions. The simulations indicate that molecule-wall collisions influence the velocity profile, which deviates significantly from the Navier-Stokes hydrodynamic prediction for micro- and mesopores. Also, the shape of the velocity profile is found to be independent of the applied pressure gradient in micropores. The results indicate that the velocity profile is uniform for pore sizes less than 2 nm (micropores) where the transport is mainly due to molecular streaming or Knudsen diffusion and, to a lesser extent, molecular diffusion. As pore sizes increase to 10 nm, parabolic profiles are observed due to the reduced interaction of gas molecules with the pore walls. A 3D pore network, representative of porous carbon-based materials, has been generated atomistically using the Voronoi tessellation method. Simulations have been carried out to determine the effect of the pore structure and modeled viscosity on permeability and Klinkenberg parameters. The use of the bulk-phase viscosity for estimating the permeability of CO_2 in units of Darcy in a 3D micropore network is not an appropriate assumption as it significantly underestimates the CO_2 permeability. On the other hand, since the transport properties of CH_4 are less influenced by the pore walls compared with CO_2, the use of the bulk-phase CH_4 viscosity estimates are a reasonable assumption. © *2013 American Institute of Physics*. [http://dx.doi.org/10.1063/1.4790658]

I. INTRODUCTION

Transport and separation of carbon dioxide (CO_2) in microporous carbon-based materials is a problem of industrial importance, particularly for the mitigation of greenhouse gas emissions, which is currently of fundamental and practical interest. Carbon capture and storage (CCS) has the capacity to potentially mitigate gigatons of CO_2 emissions. Among the various geologic formations investigated, some of which include deep saline aquifers, depleted oil/gas reservoirs, and unmineable coalbeds, each has different storage capacities.[1] Depleted oil and gas reservoirs are estimated to have a storage capacity of 675–900 $GtCO_2$, with deep saline formations having a potential storage capacity of at least 1000 $GtCO_2$.[2] Although the capacities of unmineable coal seams are significantly lower (i.e., 3 $GtCO_2$ up to 200 $GtCO_2$)[2] than saline aquifers and depleted oil and gas reservoirs, they are particularly useful for enhanced coal-bed methane recovery (ECBM) applications. Another advantage of storing CO_2 in coalbeds is that they are often close in proximity to electricity generation sources.[3,4] However, obstacles including technical maturity and cost, as well as public perception, regulatory aspects and environmental issues have thus far hindered wide-scale deployment of this strategy.[2]

It is important to understand the transport properties of CO_2 and its interaction with its local surroundings on the molecular-scale to design efficient and reliable strategies for carbon storage at full-scale. Fundamental understanding of the microstructure of coal and gas shale and their influence on the transmissibility of methane is of great importance in the recovery of this valuable resource.[5] To understand the molecular processes relevant to storage of CO_2 in unmineable coal seams or gas shale with enhanced methane recovery, gas transport phenomena in the matrix require further investigation.

Although theories of gas transport in porous media have been used and applied for many years, specific complexities such as material and pore size heterogeneities make each problem and case unique. Some examples include, but are not limited to gas transport through tight sands, coal-bed methane, and unconventional shale gas reservoirs, in which more reliable and precise modeling are required.[6–8] Each of these example systems is composed of a network of very small pores, which are partially responsible for uncertainties in permeability and flux estimates based upon Navier-Stokes approaches.

Classical Navier-Stokes hydrodynamics is known to describe the macroscopic flow of simple fluids.[9] Flow through typical porous media composed of large pores (i.e., on the order of microns) such as sandstones of depleted oil and gas reservoirs may be modeled using Darcy's law derived from the Navier-Stokes equation by using a formal averaging procedure,[10,11] in which the continuum flow assumption is valid. However, when temperature and density vary appreciably on a scale comparable to the molecular mean free path,

a)Author to whom correspondence should be addressed. Electronic mail: jen.wilcox@stanford.edu.

these equations break down.[12] Therefore, flow through very narrow channels or pores may not be accurately described based upon these traditional macroscopic approaches.[9] As pores become smaller the flow no longer obeys Darcy's law and correction factors associated with the transport may be required.[6,13]

Interestingly, in small pores unlike in large pores (where continuum flow occurs), the gas velocity at the walls is *non-zero* and predicted gas transport is somewhat enhanced as the gas flow transitions from a parabolic velocity profile to plug-flow.[14] Gas molecules are transported along the walls by molecular streaming or Knudsen diffusion due to gas slippage or surface hopping of adsorbed gas molecules.[14] The hydrodynamic boundary condition of methane and argon flowing in graphene nanochannels were previously examined using molecular dynamics (MD) simulations, and the no-slip boundary condition was shown to be violated for fluids confined by graphene surfaces owing to their atomic smoothness and lyophobicity.[15] Using a lattice Boltzmann simulation approach, previous investigations have shown that due to strong gas-solid interactions, molecular streaming along carbon pore walls dominates the gas transport mechanism in kerogen.[14] Also, It has been shown that the shape of the velocity profile is independent of the applied pressure gradient in small pores, while classical Navier-Stokes behavior is approached for channel widths greater than ~10 molecular diameters.[9]

Within the current work we investigate the gas slippage and simulated viscosity effects for a model gas confined to micro- and mesopores. The density and streaming velocity profiles of the gas undergoing a pressure gradient along the pore length are examined in detail. Klinkenberg[16] was the first to apply results of gas slippage theory to the petrophysical domain, and assumed that the porous medium consists of a bundle of equidimensional pore capillaries of radius r and argued that, in capillaries with a diameter comparable to the mean free path of the gas, interactions between the gas molecules and the capillary walls contribute to the forward movement of gas molecules in the transport direction. This "gas slippage" reduces viscous drag and increases permeability. Under the assumptions of Klinkenberg, a thin layer exists close to the pore wall in which only collisions between the gas and wall take place, with gas-gas interactions ignored.[17] Klinkenberg noted that in the pore capillary system the mean free path (λ) is inversely proportional to the mean pressure (p_m) and combined Poiseuille's law for gas flow in capillaries with Darcy's law for flow in porous media, to obtain the Klinkenberg equation

$$k_g = k_\infty \left(1 + \frac{b}{p_m}\right), \quad (1)$$

where k_∞ is the permeability at infinite pressure (liquid permeability) and b is referred to as the gas slippage factor.[16,18]

As previously described, the mean free path is inversely proportional to the mean pressure, thus at lower pressures the mean free path increases, and the slippage effect and subsequent gas permeability are enhanced. At higher mean pressures, the slippage effect is suppressed and permeability is reduced until at infinite mean pressure the mean free path is reduced to zero at which point the gas molecules are considered to behave as a liquid, with the gas and inert liquid permeability, k_∞, becoming equivalent.[18]

Molecular simulation investigations are carried out in the current work and are based on non-equilibrium molecular dynamics (NEMD), a technique ideally suited for the experimental situation in which an external driving force, such as a chemical potential or pressure gradient, is applied to a given pore or pore network. A dual control-volume-grand-canonical molecular dynamics (DCV-GCMD) technique, which has been used extensively[19–41] has been utilized in the current work.

To date there exists little fundamental knowledge regarding gas transport and slippage in carbon-based porous systems on the molecular scale. The current investigation was designed to shed light on the details of transport processes at the atomistic level and to demonstrate the possible use of this common technique in the field of CO_2 transport and storage. This work represents the steps required for a deeper understanding of the phenomena involved during the transport of gas mixtures in carbon-based materials. The results indicate that molecular phenomena play a significant role on the transport of gases in confined spaces, and offer unique insight into the behavior and transport of gases inside porous carbon-based materials.

II. COMPUTATIONAL METHODS

A. Carbon slit pore

A single carbon slit pore was modeled to investigate the Klinkenberg effect and gas slippage. A schematic representation of the pore model is shown in Figure 1, in which the origin of the coordinate system lies at the center of the pore. The two carbon walls are located at the top and bottom xy planes. The external driving force is a chemical potential or, equivalently, a pressure gradient applied in the x-direction. The system is divided into three regions: the h- and l-regions represent, respectively, the two control volumes (CVs) exposed to the bulk gas at high (upstream) and low (downstream) chemical potential or pressure, while the middle region represents the pore. The pore's length is nL with n defined as an integer. In our calculations we used $n = 1$. Periodic boundary conditions were employed only in the y-direction. The slit pore model has been used in previous related studies in which gas transport in carbon molecular sieve membranes was investigated.[38–41] Surface roughness was not taken into account in this initial study and as such the pore's walls are assumed to be smooth (structureless).[34–37]

B. Three-dimensional (3D) carbon-based pore network

To predict the gas permeabilities using a more realistic 3D carbon-based porous structure, the pore network model was generated by the Voronoi tessellation of a solid material composed of hundreds of thousands of atoms, and by designating a fraction of the Voronoi polyhedra as the pores. The model allows for the investigation of the effect of the morphology of the pore space, i.e., its pore size distribution

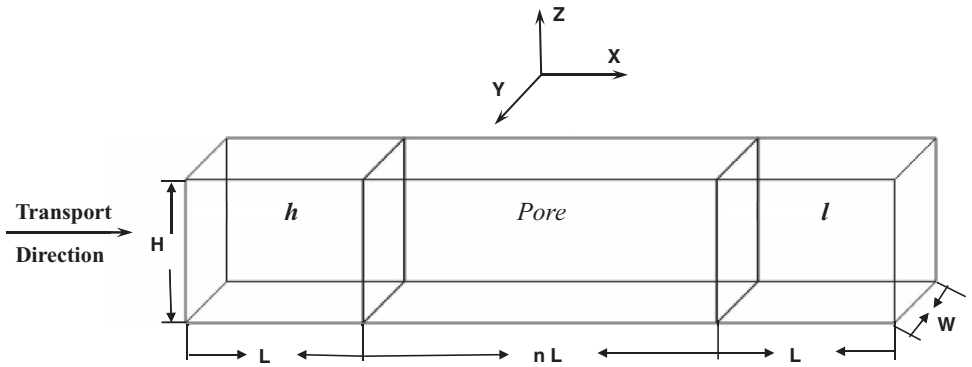

FIG. 1. Schematic of the slit pore model used in the simulations. The *h* and *l* regions represent the high- and low-pressure control volumes, respectively.

and pore connectivity, on the gas transport of CH_4 and CO_2 components.[42] In this method, described in detail in previous work,[42] we begin with a 3D cell of carbon atoms with a structure corresponding to graphite so that the number density of carbon atoms is 114 nm^{-3} and the spacing between the adjacent graphite layers in the z direction is 0.335 nm. The size of the initial graphite cell is 102, 103, and 103 Å in x, y, and z directions, respectively, and consists of 124,992 carbon atoms. Periodic boundary conditions are applied in all directions. The graphite cell is then tessellated through the insertion of a given number of Poisson points at random positions inside the simulation cell, each of which is used for constructing a 3D Voronoi polyhedron, such that every point inside each polyhedron is closer to its own Poisson point than to any other Poisson point. The pore space is then generated by fixing its desired porosity and selecting a number of polyhedra that may be chosen randomly or by first sorting and listing the polyhedra in the cell according to their sizes from smallest to largest (or vice versa), in such a way that their total volume fraction equals the desired porosity. The polyhedra, so chosen, are then designated as the pores by removing the carbon atoms comprising them, as well as those that are connected to only one neighboring carbon atom (the dangling atoms, i.e., connected to only one other atom). The remaining carbon atoms constitute the solid matrix, while the pore space consists of interconnected pores of various shapes and sizes. The equivalent radius of each polyhedron is taken to be the radius of a sphere that has the same volume as the polyhedron. The computed pore size distribution (PSD) of the pore network with the average pore size 20 Å when the porosity is 20% and the pores are selected randomly is given in the supplementary material.[43]

C. DCV-GCMD method

The DCV-GCMD method was employed to investigate the transport properties of gas molecules, which combines the MD moves in the entire system with the grand-canonical Monte Carlo (GCMC) insertions and deletions of the molecules in the two CVs. The densities, or the corresponding chemical potentials, of the components in the CVs were maintained using a sufficient number of GCMC insertions and deletions.[19,21,23,34–42] The probability of inserting a molecule of component *i* is given by

$$p_i^+ = \min\left\{\frac{Z_i V_c}{N_i + 1} exp\left(-\Delta U / k_B T\right), 1\right\}, \qquad (2)$$

where $Z_i = \exp\left(\mu_i / k_B T\right) / \Lambda_i^3$ is the absolute activity at temperature T, Λ_i, and μ_i are, respectively, the de Broglie wavelength (Λ_i) and the chemical potential of component i, k_B is the Boltzmann's constant, ΔU is the potential energy change resulting from inserting or removing a molecule, and V_c and N_i are the volume of the CV and number of atoms of component i in each CV, respectively. Similarly, the probability of deleting a molecule is given by

$$p_i^- = \min\left\{\frac{N_i}{Z_i V_c} exp\left(-\Delta U / k_B T\right), 1\right\}. \qquad (3)$$

The chemical potentials were converted to equivalent pressures using a Lennard-Jones (LJ) equation of state.[44] When a molecule is inserted in a CV, it is assigned a thermal velocity selected from the Maxwell–Boltzmann distribution at the given T. Typically, 10 GCMC insertions and deletions in each CV were followed by one MD integration step. In the MD simulations, the Verlet velocity algorithm was used to integrate the equations of motion with a dimensionless time step, $\Delta t^* = 5 \times 10^{-3}$ (i.e., $\Delta t = 0.00685$ ps). The equations of motion were integrated with up to 5×10^6 time steps to ensure that steady state has been reached. Steady state was typically reached in the system after 3×10^6 time steps; however, the simulation is continued up to 5×10^6 time steps, after which the properties, such as concentration and velocity profiles, fluxes, etc., were calculated and averaged over the last 1×10^6 time steps. During the MD calculations molecules that crossed the outer boundaries of the CVs were removed. However, the number of such molecules was very small, typically about 1% of the total number of molecules deleted during the GCMC simulations. To study the transport of a gas molecule due to an applied pressure gradient, the temperature of the system was held constant at 25 °C to eliminate any contribution of the temperature gradient to the transport; hence, isokinetic conditions were maintained by rescaling the velocity independently in all the three directions. In this work the walls are rigid.

D. Potential models of the molecules and carbon walls

The molecules CO_2 and CH_4 were represented using LJ potentials and characterized by the effective LJ size and energy parameters, σ and ε, respectively.[45] We used $\sigma_{CO2} = 3.79$ Å, and $\varepsilon_{CO2}/k_B = 225.3$ K, and $\sigma_{CH4} = 3.81$ Å, $\varepsilon_{CH4}/k_B = 148.1$ K.[38] For the cross-term LJ parameters, the Lorentz-Berthelot mixing rules were used to compute the size and energy parameters of the unlike molecules.[46]

The gas-gas interactions were modeled with the cut-and-shifted LJ 6–12 potential with a cut-off distance $r_c = 9.5$ Å ($2.5\sigma_{CH4}$).[36,38–42] As previously mentioned, we utilized smooth pore walls described by the 10-4-3 Steele potential,

$$U_{iw}(z) = 2\pi\rho_c\varepsilon_{iw}\sigma_{iw}^2\Delta \times \left\{\frac{2}{5}\left(\frac{\sigma_{iw}}{z}\right)^{10} - \left(\frac{\sigma_{iw}}{z}\right)^{4} - \frac{\sigma_{iw}^4}{3\Delta(0.61\Delta + z)^3}\right\}, \quad (4)$$

which was used to calculate the interaction between a gas molecule and the wall, where $\Delta = 0.335$ nm is the space between the adjacent carbon layers, $\rho_c = 114$ nm^{-3} is the number density of carbon atoms in the layer, z is the distance from the wall, and σ_{iw} and ε_{iw} are the LJ parameters between the walls and molecule i. The dimensions of the pore used are $W = 76.2$ Å ($20\sigma_{CH4}$) and $L = 152.4$ Å ($40\sigma_{CH4}$), while the pore sizes (heights) may vary from micropores with $H = 11.4$ ($3\sigma_{CH4}$) and 19.0 Å ($5\sigma_{CH4}$) to mesopores with $H = 26.7$ ($7\sigma_{CH4}$), 38.1 ($10\sigma_{CH4}$), 57.1 ($15\sigma_{CH4}$), 76.2 Å ($20\sigma_{CH4}$), and 100 Å ($26.2\sigma_{CH4}$) to assess the effect of the pore sizes on the transport phenomena.

We computed several quantities of interest, including the velocity profiles, $v_i^x(z)$, of the component i along the z-direction at the particular value of x and the density profiles of the component i along the x- and z-directions, $\rho_i^z(x)$ and $\rho_i^x(z)$, respectively. To calculate $\rho_i^z(x)$, the simulation box in the x-direction was divided into grids of size 3.81 Å (σ_{CH4}), and for each MD step the density profiles $\rho_i^z(x)$ were obtained by averaging the number of molecules of component i over the distance 3.81 Å. A similar procedure was used for computing $\rho_i^x(z)$ and $v_i^x(z)$, with the averaging carried out over small distances of 0.38, 0.64, 0.89, 1.27, 1.90, 2.54, and 3.33 Å with corresponding pore sizes of H = 11.4, 19.0, 26.7, 38.1, 57.1, 76.2, and 100 Å, respectively. As discussed next in greater detail, these quantities are important in understanding the gas transport properties in nanoconfined pore systems.

In addition, for each component i the flux, J_i, in the direction of the applied pressure gradient was calculated by measuring the net number of gas molecules crossing a given yz plane. The permeability, K_i, of component i was then calculated using

$$K_i = \frac{J_i}{\Delta P_i/nL} = \frac{nLJ_i}{\Delta P_i}, \quad (5)$$

where $\Delta P_i = x_i\Delta P$ is the partial pressure drop for component i along the pore, with x_i being the mole fraction of component i, and ΔP is the total pressure drop imposed along the pore.

E. Viscosity modeling using GCMC and MD methods

To calculate the viscosity using MD, the adsorption isotherms of CH_4 and CO_2 in the pore model were calculated using the conventional GCMC simulations. The average number densities of CH_4 and CO_2 molecules obtained from GCMC simulations were then used as the input for the canonical (*NVT*) MD simulations to predict the self-diffusion coefficients of CH_4 and CO_2 inside the pore network model to calculate the viscosity using molecular simulation as described below.

In the GCMC simulations the chemical potential, temperature, and pore volume are fixed with periodic boundary conditions applied in all directions. The initial configuration was randomly generated with a few number of gas molecules inside the simulation box. The Metropolis algorithm was used to create the new configurations by changing the position of a randomly selected gas molecule and by insertion or removal of gas molecules from the pore network structure. For each combination of chemical potential and temperature, 4×10^6 configurations were generated. Half of the configurations were used to reach system equilibrium and the other configurations were divided into 200 intervals to average the thermodynamic properties.[47]

In the MD simulations, the Verlet velocity algorithm was used to integrate the equations of motion with a dimensionless time step, $\Delta t^* = 5 \times 10^{-3}$ (i.e., $\Delta t = 0.00685$ ps). The periodic boundary conditions were imposed in all directions with the temperature held at 25 °C. The initial configurations allowed for equilibration up to 1,000,000 time steps and then another 100,000 steps used to sample and collect the information for the velocity autocorrelation function (ACF) equations and diffusion coefficients.

The self-diffusion coefficients were calculated from the Green-Kubo relation in three dimensions using

$$D = \frac{1}{3}\int_0^\infty \langle v_i(t).v_i(0)\rangle dt, \quad (6)$$

where N is the total number of molecules, and $v_i(t)$ is the velocity of molecule i at time t. The bracketed quantity represents the velocity ACF. The viscosity then was estimated from the Einstein relation using

$$\mu = \frac{k_B T}{3\pi d D}, \quad (7)$$

where k_B is the Boltzmann's constant, T is the temperature, d *is* the diameter of the gas molecule, and D is the self-diffusivity estimated from Eq. (6). In what follows, we present and discuss the results of our simulations. The temperature of the system was held constant at 25°C.

III. RESULTS AND DISCUSSION

Non-equilibrium molecular dynamics simulations modeling the transport properties of pure CH_4 and CO_2 and their equimolar mixtures were conducted. Figure 2 represents the time-averaged velocity profiles, $v_i^x(z)$, for pure CH_4 and CO_2 in the yz planes (perpendicular to the direction of the applied pressure gradient) at 1/4, 1/2, and 3/4 of the pore length. As Figure 2 shows, the velocity profiles of both CH_4 and CO_2

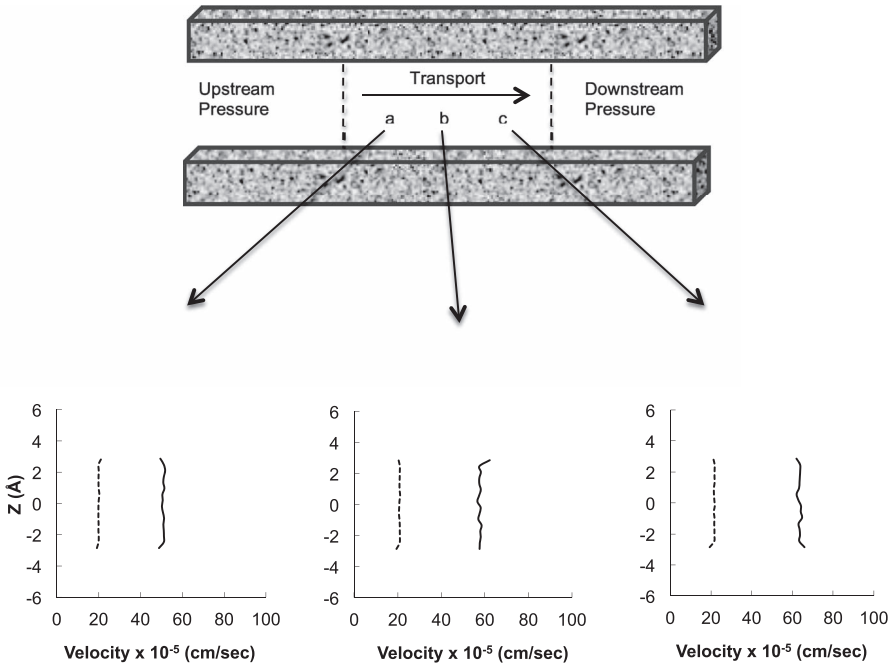

FIG. 2. Velocity profiles $v^x(z)$ of pure CH_4 (solid curves) and CO_2 (dotted curves) in pore's cross sections at 1/4 (a), 1/2 (b), and 3/4 (c) of the pore length. The pore size is 11.4 Å and the upstream and downstream pressures are 3 and 1 atm, respectively.

deviate from Navier-Stokes hydrodynamic predictions. The parabolic profile is replaced with a uniform velocity profile (plug-flow) along the entire length of the pore, as molecular streaming becomes the dominant transport mechanism due to the increased pore-wall effects.[14]

Also, the velocity profiles of both CH_4 and CO_2 are *non-zero* at the closest layer to the wall. We may then conclude that the molecule-wall collisions likely influence the velocity profile and, due to the increased pore-wall effects, molecular streaming becomes dominant. A thin layer adjacent to the wall exists where only collisions of gas molecules with the pore wall occur and gas-gas collisions may be ignored, which is consistent with the theory of Klinkenberg.[17] In addition, the velocity of CH_4 molecules is larger than that of CO_2 due to the enhanced adsorption effect of CO_2 on the carbon surface and the resulting higher mobility of CH_4 molecules in the pores. Moreover, as the gas approaches the lower pressure along the pore the velocity increases, as expected, which is more noticeable for CH_4 molecules than CO_2 molecules.

Figure 3 represents the same CH_4 and CO_2 velocity profiles as shown in Figure 2 in an equimolar mixture. All the qualitative features of the profiles are similar to those shown in Figure 2, except that the velocity profiles of both components in the mixture are equal in the pore. This phenomenon can be attributed to the fact that the CO_2 molecules have a shielding effect which is stronger for tighter pores, in that, they reduce the mobility of CH_4 molecules, resulting in the uniform transport of both components in the gas mixture along the pore.

To better understand the distributions of CH_4 and CO_2 in the pore, Figure 4 presents the time-averaged densities, $\rho_i^x(z)$, of CH_4 and CO_2 in an equimolar mixture in the yz planes at 1/4, 1/2, and 3/4 of the pore length. As shown, each component in the gas mixture forms only two adsorbed layers close to the walls, which indicates that most gas molecules are distributed near the pore walls. Another feature of Figure 3 worth mentioning is that the density of CO_2 is higher than that of CH_4, an effect caused by the relative adsorption affinities of the gases for the carbon surface. The energy contribution of CO_2-carbon interactions is greater than that of CH_4-carbon interactions, i.e., the carbon atom of the pore surface is more attractive to CO_2 than to CH_4 molecules. This is consistent with CO_2 having a significant quadrupole moment (i.e., 13.4 C m^2), whereas CH_4 is nonpolar.[49]

Figure 5 presents the time-averaged density profiles, $\rho_i^z(x)$ (averaged in the *yz* planes), of CH_4 and CO_2 in an equimolar mixture as functions of *x* along the pore, defined as the region, $-76.2 < x < 76.2$ Å, computed by averaging the results over the last 1,000,000 time steps. In this and subsequent figures, the vertical dashed lines indicate the boundaries of the pore region. The density profiles are essentially flat in the two CVs, with numerical values that match those obtained by the GCMC method at the same conditions, indicating that the chemical potentials in the two CVs have been properly maintained during the NEMD simulations. As can be seen in Figure 5, in the transport region, i.e., $-76.2 < x < 76.2$ Å, the densities for both components decrease along the pore, which is expected. The density of CO_2 is larger than that of CH_4 due to the affinity of CO_2 for carbon surfaces, as described previously and in earlier studies.[3,50] However, the density profiles in the transport region are not linear due to the existence of the overall bulk pressure gradient (or an overall non-zero streaming velocity). The diffusive and convective fluxes make up the total flux, which result in a nonlinear profile. These features

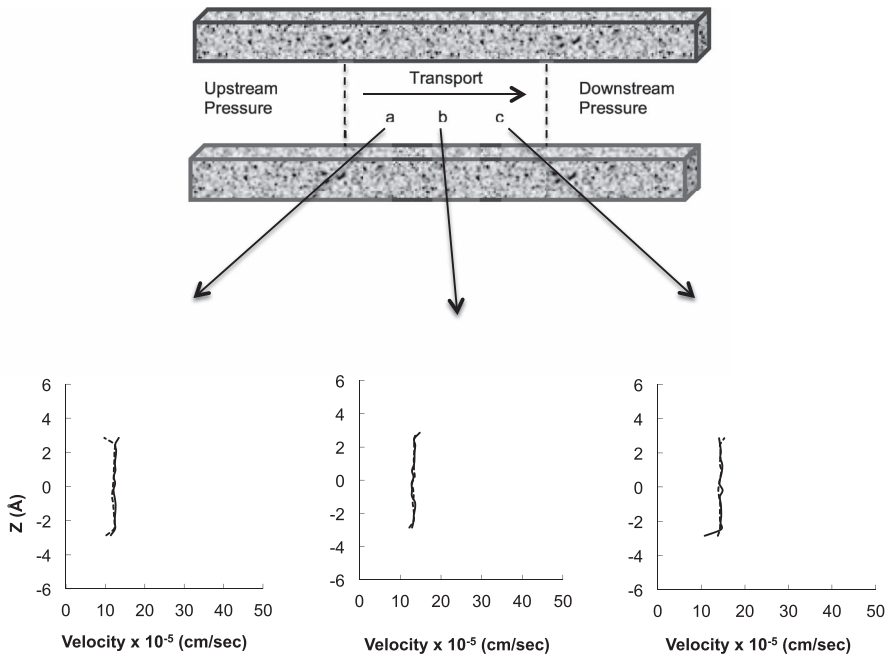

FIG. 3. Velocity profiles $v^x(z)$ of CH_4 (solid curves) and CO_2 (dotted curves) in an equimolar mixture in the pore's cross sections at 1/4 (a), 1/2 (b), and 3/4 (c) of the pore length. The pore size is 11.4 Å and the upstream and downstream pressures are 3 and 1 atm, respectively.

are clearly seen in Figure 6, where we show snapshots of the same pore and the distribution of the gas molecules for the same mixture as in Figure 5, obtained at steady state after 5 $\times$ 10^6 time steps. From this figure it is evident that the densities of both components in the mixtures decrease from left to right, and the number of the CO_2 molecules in the pore is larger than the number of CH_4 molecules.

It is important to determine the pore size depicting the transition from plug-flow to a parabolic velocity profile so that accurate transport properties may be incorporated into larger scale reservoir models. To determine the effect of pore size on the velocity profiles, the pore size was increased from micro- to mesopores. Figure 7 shows the time-averaged velocity profiles, $v_i^x(z)$, of CH_4 and CO_2 in an equimolar mixture at the center of the pore under precisely the same conditions as Figure 3, except that the pore sizes investigated in Figure 7 are 19.0, 26.7, 38.1, and 57.1 Å. The results indicate that, as the pore size increases, the pore becomes less packed and as molecular transport through the pore is less hindered, the gas velocity increases. This is more noticeable for CH_4 molecules than CO_2 molecules as CH_4 is more evenly distributed throughout the pore. As a result, by increasing the

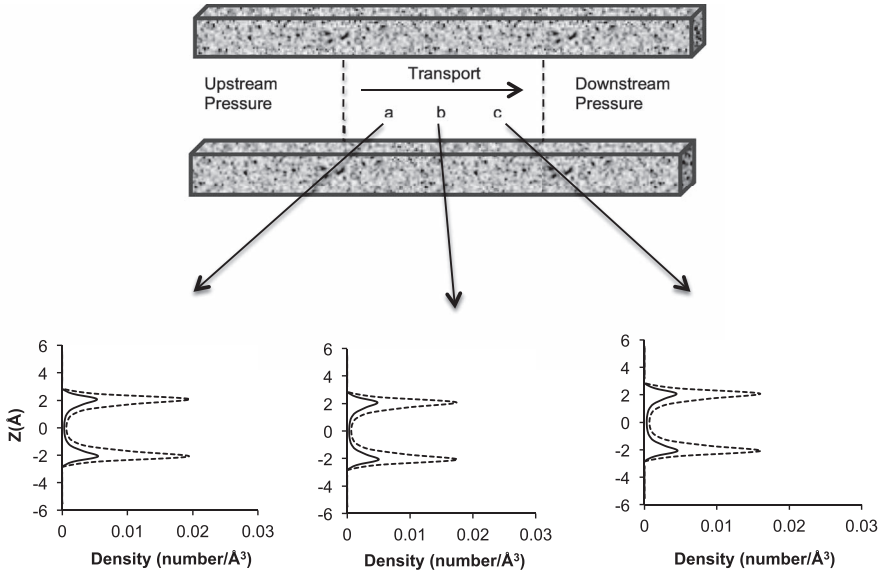

FIG. 4. Density profiles $\rho^x(z)$ of CH_4 (solid curves) and CO_2 (dotted curves) in an equimolar mixture in the pore's cross sections at 1/4 (a), 1/2 (b), and 3/4 (c) of the pore length. The pore size is 11.4 Å and the upstream and downstream pressures are 3 and 1 atm, respectively.

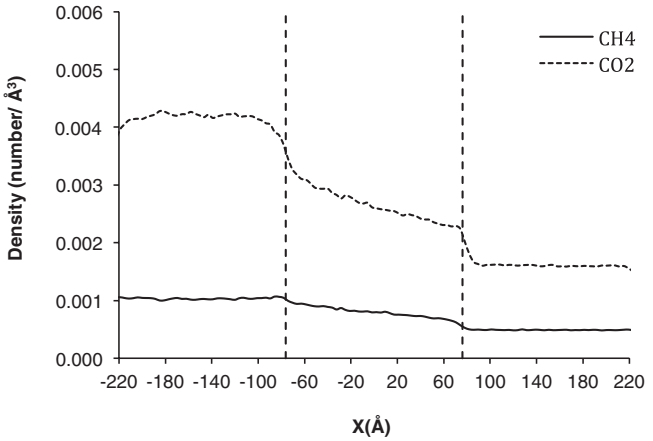

FIG. 5. Time-averaged density profiles $\rho^z(x)$ of CH_4 (solid curve) and CO_2 (dotted curve) in an equimolar mixture in the transport direction x. The pore size is 11.4 Å and the upstream and downstream pressures are 3 and 1 atm, respectively. Dashed vertical lines indicate the boundaries of the pore region.

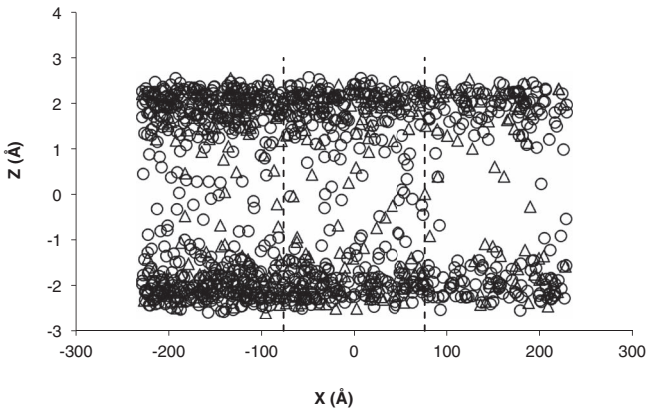

FIG. 6. A snapshot of the pore with the distributions of CH_4 (triangles) and CO_2 (circles) in an equimolar mixture, when the pore size is 11.4 Å and the upstream and downstream pressures are 3 and 1 atm, respectively. Dashed vertical lines indicate the boundaries of the pore region.

pore size the velocity of CH_4 molecules becomes larger than that of CO_2, which can be attributed to the higher adsorption of CO_2 on the carbon surface, as described previously, and the higher mobility of CH_4 molecules in the larger pores. This implies that as pores become larger, the shielding effects and pore blocking of CH_4 molecules caused by CO_2 molecules that exists in the smaller pores as described previously in Figure 3, decreases. Moreover, it seems that as pore size increases, the velocity profile becomes more parabolic and classical Navier-Stokes behavior is approached. The velocity profile of CO_2 is affected only weakly by the change in pore size, while the velocity profile of CH_4 appears to depend rather strongly on the pore size. These features should be compared with those encountered with smaller pores when the gas molecule-wall collisions influence the velocity profile.

Figure 8 shows the time-averaged velocity profiles, $v_i^x(z)$, and density profiles, $\rho_i^x(z)$, of CH_4 and CO_2 in an equimolar mixture in the yz planes at 1/4, 1/2, and 3/4 of the pore length for a pore size of 76.2 Å. All of the qualitative features of the profiles are similar to those shown in Figures 7 and 4, except that in the larger pores the velocity profile is more parabolic throughout the pore, especially for the CH_4 gas molecules. Also, when pore size is increased, the density profiles of the two components in the pore are lower. This is due to decreased adsorption onto the carbon walls in the larger pores, where the gas molecules form only two adsorbed layers near the pore walls, leaving the center of the pore nearly empty. Similar to Figure 3, the results show that the velocities of both components increase as the pressure gradient decreases along the pore, as described previously.

As the pore size increases to 100 Å [10 nm] parabolic velocity profiles are observed due to the reduced interaction of gas molecules with the carbon pore surfaces. Figure 9 shows the time-averaged velocity profiles, $v_i^x(z)$, of pure CH_4 and CO_2 as well as in an equimolar mixture of the two components for a 100 Å pore size when the upstream and downstream pressures are 30 and 10 atm, respectively. The time-averaged velocity profiles of pure CH_4 and CO_2 as well as in an equimolar mixture of the two components for a 100 Å pore size when the upstream and downstream pressures are 3 and 1 atm, respectively, are also given in the supplementary material.[43]

Figure 10 shows the time-averaged velocity profiles, $v_i^x(z)$, of CH_4 and CO_2 in an equimolar mixture in the center plane of a micro- and mesopore of 11.4 and 76.2 Å, respectively. The downstream pressure is fixed at 1 atm, while the upstream pressures are varied between 3 and 11 atm in order to assess the effect of the applied pressure drop ΔP on the transport behavior. In previous studies, it was shown that the shape of the velocity profile is independent of the applied pressure gradient.[9] Our results are in agreement with this in that there is no effect on the shape of the velocity profiles

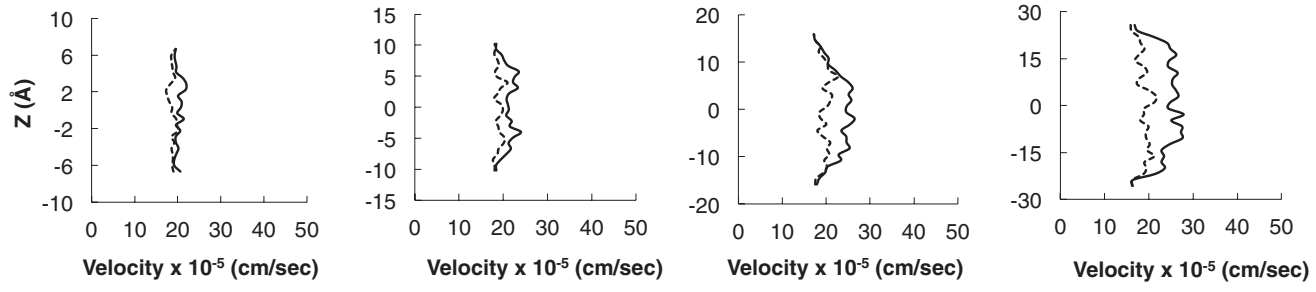

FIG. 7. Velocity profiles $v^x(z)$ of CH_4 (solid curves) and CO_2 (dotted curves) in an equimolar mixture in the pore cross section at the center of the pore. The pore sizes are 19.0, 26.7, 38.1, and 57.1 Å from left to right, respectively. The upstream and downstream pressures are 3 and 1 atm, respectively.

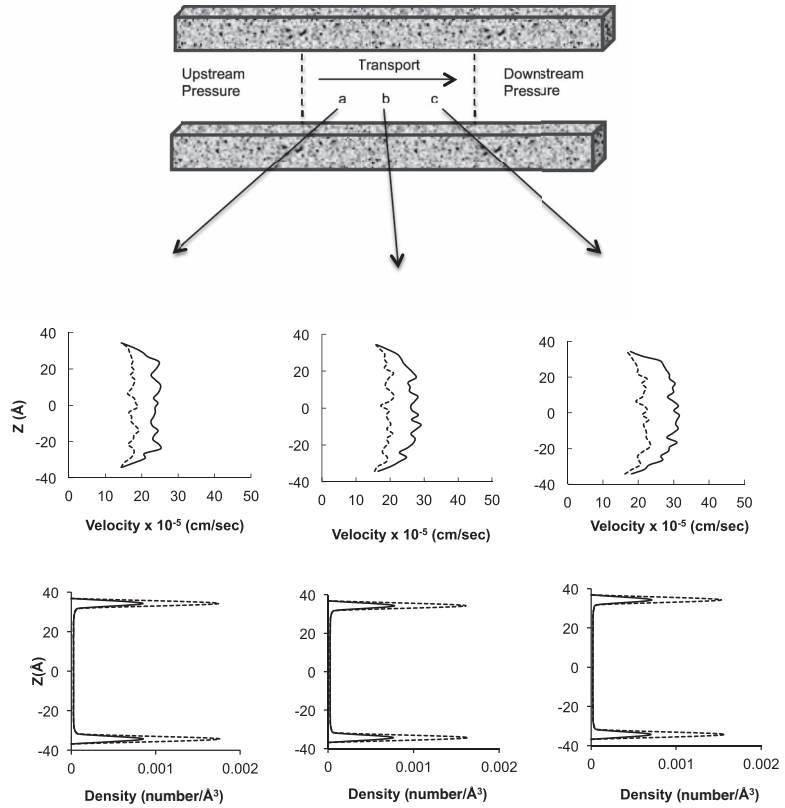

FIG. 8. Velocity profiles $v^x(z)$ (top) and density profiles $\rho^x(z)$ (bottom) of CH_4 (solid curves) and CO_2 (dotted curves) in an equimolar mixture in the pore cross section at 1/4 (a), 1/2 (b), and 3/4 (c) of the pore length. The pore size is 76.2 Å and the upstream and downstream pressures are 3 and 1 atm, respectively.

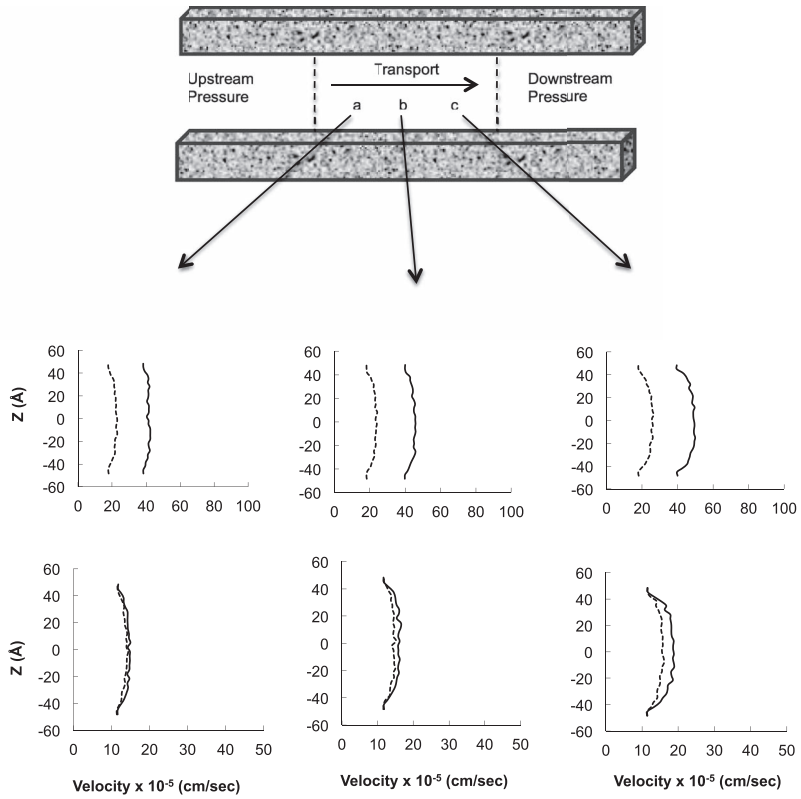

FIG. 9. Velocity profiles $v^x(z)$ of pure CH_4 (solid curves) and CO_2 (dotted curves) (top) and in an equimolar mixture (bottom) in the pore cross section at 1/4 (a), 1/2 (b), and 3/4 (c) of the pore length. The pore sizes are 100 Å and the upstream and downstream pressures are 30 and 10 atm, respectively.

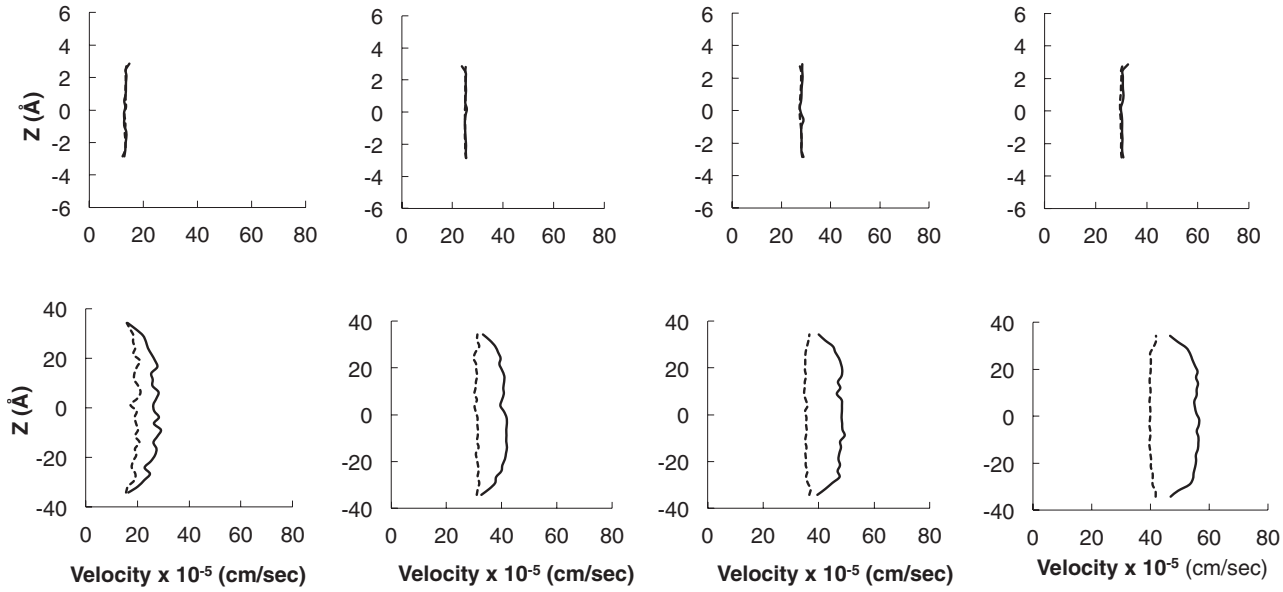

FIG. 10. Velocity profiles $v^x(z)$ of CH_4 (solid curves) and CO_2 (dotted curves) in an equimolar mixture in the pore cross section at the center of the pore. The pore sizes are 11.4 Å (top) and 76.2 Å (bottom). The downstream pressure is 1 atm, while the upstream pressures are 3, 7, 9, and 11 atm from left to right, respectively.

given a mixture of CH_4 and CO_2 in a micropore with respect to an increasing applied pressure gradient along the pore. In addition, as expected, the velocity of both components in the mixture increases with increasing overall pressure drop along the pore, as gas convection also increases. The effect of the applied pressure gradient on the velocity profiles of pure CH_4 and CO_2 gases in a micropore was also investigated and the shape of the velocity profile for both pure CH_4 and CO_2 gases also found to be independent of the applied pressure gradient in micropore.

Figure 11 presents the permeability of both components in an equimolar mixture for the same pores and conditions, as shown in Figure 10. As can be seen in this figure the permeability of both components in the mixture is larger in the micropore than in the mesopore. Also, the permeability of CO_2 is larger than CH_4 due to the affinity of CO_2 for carbon surfaces as expected, which lead to have a larger density of CO_2 in the pore that can block CH_4 molecules from passing and can be considered as shielding effects to transport.[38–41] The permeabilities of pure CH_4 and CO_2 for the same conditions as described in Figure 10 are also shown in Figure 12 with a pore size of 11.4 Å.

The effect of the pore packing and increasing pressure on the velocity profiles was also investigated. It was found that as the upstream and downstream pressures increase, with a constant pressure drop along the pore, the velocities of both components decrease due to pore packing and decreased mobility of the gas molecules. Figure 13 shows the permeabil-

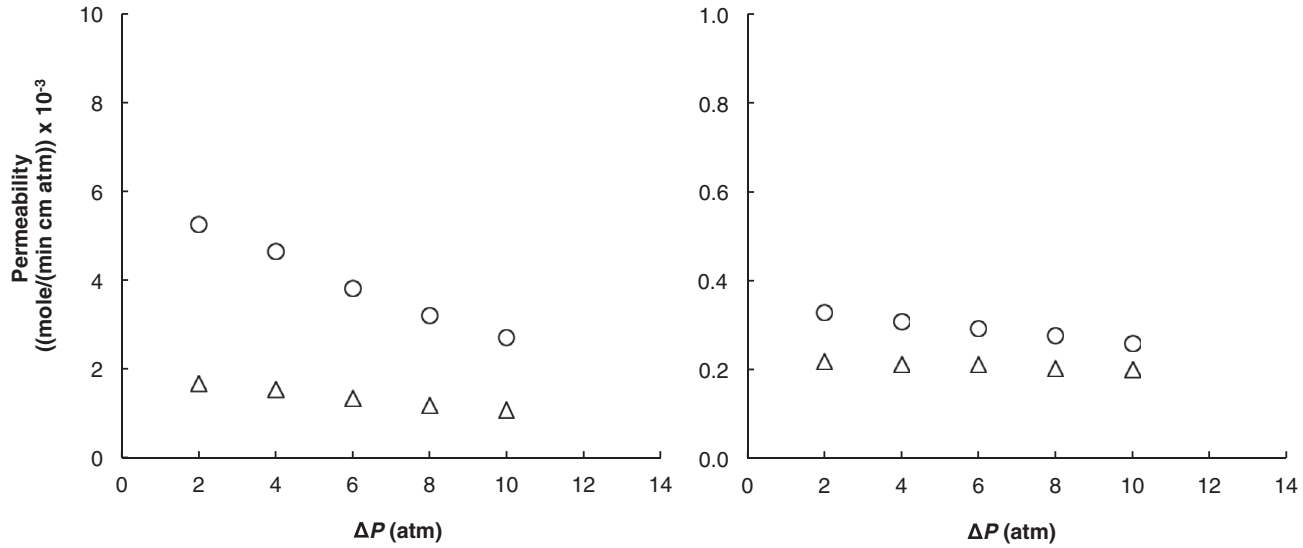

FIG. 11. The dependence of the permeability of CH_4 (triangles) and CO_2 (circles) in an equimolar mixture on the pressure drop, ΔP, applied to a pore of size 11.4 Å (left) and 76.2 Å (right). The downstream pressure is 1 atm.

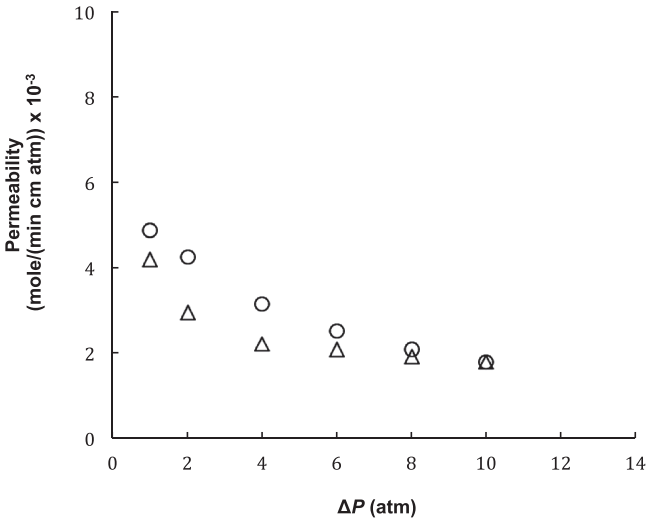

FIG. 12. The dependence of the permeability of pure CH_4 (triangles) and CO_2 (circles) on the pressure drop, ΔP, applied to a pore of size 11.4 Å. The downstream pressure is 1 atm.

ity of both components in an equimolar mixture with a pressure drop of 2 atm and upstream pressures of 3, 5, 7, 9, and 11 atm. Similar to Figure 11, the permeability of both components in the mixture is greater in the micro- than the mesopore, and the permeability of CO_2 is greater than that of CH_4. In addition, by increasing the upstream and downstream pressures but maintaining the same pressure drop along the pore, the permeability of both components decreases. This effect is more noticeable in the micropore. This phenomena can be defined based on the theory of Klinkenberg in that at the lower pressures the mean free path increases thereby increasing the slippage effect and leading to enhanced gas permeability, while at the higher mean pressures the slippage effect is suppressed leading to reduced permeability.

Previous studies indicate that in a realistic disordered porous natural system, the gas transport is dominated by the geometrical and topological characteristics of the material.[36,39,42,51] As a result, the use of a single carbon slit pore as used in this work to model the velocity profiles and slip boundary conditions, is a grossly inadequate model to predict gas permeability in real porous natural systems. A more accurate approach involves the use of a three-dimensional molecular pore network for modeling gas transport in porous media. To predict the CH_4 and CO_2 permeabilities using a more realistic 3D carbon-based porous structure, the 3D pore network model was generated as described earlier. The porosity in the generated 3D pore network is 20% and the pores are selected randomly, with average pore size of 20 Å. The number of inserted Poisson points in the simulation cell is 240.

In previous studies it has been shown that the viscosity of confined fluids is dependent on the structure and pore diameter, which is often different from the viscosity of the bulk system.[52,53,48] To investigate the effect of varying viscosity on the transport, the adsorption isotherms of CH_4 and CO_2 in the generated pore network structure were calculated using the conventional GCMC simulations. The average number densities of gas molecules obtained from GCMC simulations are then used as the input for the canonical (*NVT*) MD simulations to predict the self-diffusion coefficients using Einstein and Green-Kubo relations to calculate the viscosity theoretically as described previously. The velocity ACF of pure CH_4 and CO_2 in the pore network model was first simulated and found that after a short time the velocity ACF declines sharply and then fluctuates around zero.[48,54] The velocity autocorrelation function of pure CH_4 and CO_2 in the pore network at 20 atm is given in the supplementary material.[43]

Then, the self-diffusivities of pure CH_4 and CO_2 in the pore network model obtained from Eq. (6), exhibiting a higher self-diffusivity for CH_4 than CO_2 as expected due to the higher adsorption affinity of CO_2 on the carbon surface of the pore. The self-diffusivities of pure CH_4 and CO_2 in the pore network model are given in the supplementary material.[43] The

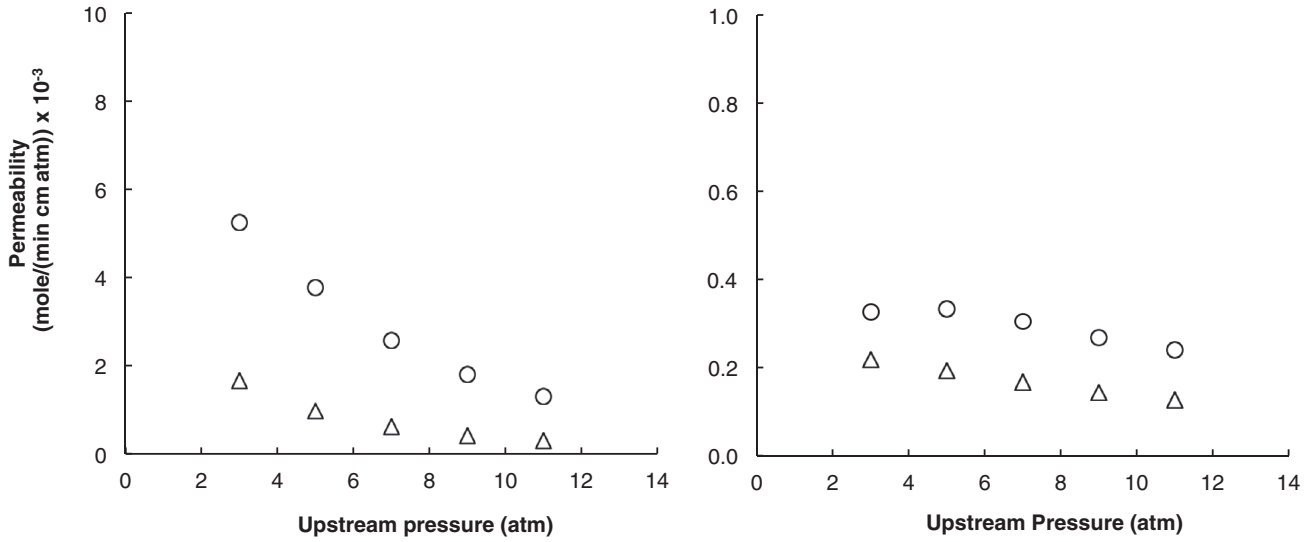

FIG. 13. The dependence of the permeability of CH_4 (triangles) and CO_2 (circles) in an equimolar mixture on the upstream pressure applied to a pore of size 11.4 Å (left) and 76.2 Å (right). The pressure drop applied to the pores is 2 atm.

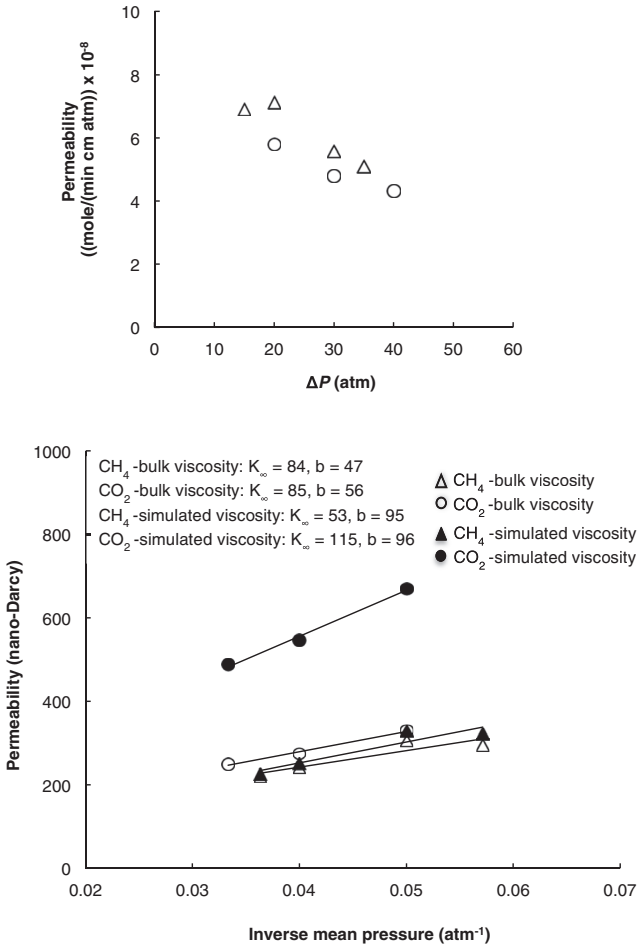

FIG. 14. The dependence of the permeability of pure CH_4 (triangles) and CO_2 (circles) on the pressure drop, ΔP, (top) and inverse mean pressure (bottom) applied to the pore network. The downstream pressures are fixed at 10 (atm). The average pore size and the porosity of the pore network is 20 Å, and 20%, respectively.

self-diffusivities are then used to calculate the viscosity using Eq. (7).

Figure 14 represents the dependence of the permeability of pure CH_4 and CO_2 on the pressure drop, ΔP, and inverse mean pressure applied to the generated pore network model as described previously. The downstream pressure is fixed at 10 atm, while the upstream pressures are varied. The gas permeabilities have been converted using the bulk viscosity and also modeled viscosities, to convert from generalized permeability units to "nano-Darcy" units which is a common unit used in petroleum-based fields, and the slippage factor b and k_∞ have been calculated based on Eq. (1) as previously described. The results in Figure 14 indicate that the effect of the viscosity on the CO_2 permeabilities is more noticeable than those of CH_4, which results in an increased permeability estimate for CO_2 when reporting permeability in Darcy units using modeled viscosity. On the other hand, since CH_4 is less influenced by the pore walls compared with CO_2, the use of the bulk-phase CH_4 viscosity is a reasonable assumption.

IV. CONCLUSIONS

The Klinkenberg effect and slip boundary conditions have been investigated through the molecular simulation of pure CH_4 and CO_2 and their equimolar mixtures in slit micro- and mesopores. The effect of the pore size on the transition from parabolic to plug-flow velocity profiles was examined. The simulations indicate that molecule-wall collisions influence the velocity profile, which deviates significantly from the Navier-Stokes hydrodynamic prediction, with slip boundary conditions for micro- and mesopores. In addition, the shape of the velocity profile is found to be independent of the applied pressure gradient in micropores. The results in this paper indicate that the velocity profile is uniform for pore sizes less than 2 nm (micropores) where the transport is mainly due to molecular streaming and, to a lesser extent, molecular diffusion. As pore sizes increase to 10 nm parabolic velocity profiles will be observed due to reduced interactions between the gas molecules and carbon pore surfaces. The 3D pore network representing carbon-based porous media has also been generated atomistically using the Voronoi tessellation method to determine the effect of the pore structure and modeled viscosity on the permeability and Klinkenberg parameters. To accurately predict the transport properties, it is important to simulate a realistic physical model of CO_2 molecules especially for systems where the size of the pores is commensurate with the size of the gas molecules and significant hindrance effects are observed. The effect of CO_2 model, as a flexible molecule, will be investigated in the future work. In addition, more complex molecular models of graphite structures containing local charge and defect sites within the pores, in addition to the inclusion of chemical functional groups inside the cavities to generate a more realistic model of natural systems of interest, such as coal and gas shales, will be considered in the future work as well. These results will potentially have important implications on CO_2 transport in carbon-based materials and geologic formations, such as unmineable coal seams or gas shale with enhanced methane recovery, and may provide an understanding of the limitations of the use of bulk-phase fluid viscosities to model transport properties for nanoconfined fluids.

ACKNOWLEDGMENTS

We are grateful to the Department of Energy – National Energy Technology Laboratory for support of this work. Additionally, we wish to acknowledge discussions with Professor Mark Zoback and Professor Anthony Kovscek, which have helped us to advance this research. The computations were carried out on the Center for Computational Earth and Environmental Science (CEES) cluster at Stanford University. Also, we would like to thank Dennis Michael for his administration of CEES and assistance in the installation of our simulation codes.

[1]S. Benson and P. Cook, *Intergovernmental Panel on Climate Change, Special Report on Carbon Dioxide Capture and Storage: Underground Geological Storage* (Cambridge University Press, Cambridge, England, 2005), Chap. 5, p. 196.
[2]B. Metz, *IPCC Special Report on Carbon Dioxide Capture and Storage* (Cambridge University Press, Cambridge, 2005).
[3]Y. Liu and J. Wilcox, Environ. Sci. Technol. **45**, 809 (2011).
[4]J. Wilcox, *Carbon Capture* (Springer, New York, 2012).
[5]P. D. Gamson, B. B. Beamish, and D. P. Johnson, Fuel **72**, 87 (1993).

[6]T. Ertekin, G. R. King, and F. C. Schewerer, SPEFE **1**, 43 (1986).
[7]A. Chawathe, T. Ertekin, and A. Grader, *SPE Annual Technical Conference and Exhibition* (Society of Petroleum Engineers, Denver, CO, 1996), pp. 565–573.
[8]J. Jalali and S. D. A. Mohaghegh, *SPE Eastern Regional Meeting, Paper No. 91414* (Society of Petroleum Engineers, Charleston, WV, 2004).
[9]K. P. Travis, B. D. Todd, and D. J. Evans, Phys. Rev. E **55**, 4288 (1997).
[10]S. P. Neuman, Acta Mech. **25**, 153 (1977).
[11]S. Whitaker, Transp. Porous Media **1**, 3 (1986).
[12]I. Bitsanis, T. K. Vanderlick, M. Tirrel, and H. T. Davis, J. Chem. Phys. **89**, 3152 (1988).
[13]F. O. Jones and W. W. Owens, J. Pet. Technol. **32**, 1631 (1980).
[14]Y. Akkutlu and E. Fathi, SPE Journal **17**, 1002 (2012).
[15]S. K. Kannam, B. D. Todd, J. S. Hansen, and P. J. Daivis, J. Chem. Phys. **135**, 144701 (2011).
[16]L. J. Klinkenberg, API Drill. & Prod. Prac. **41**, 200 (1941).
[17]M. C. Bravo, J. Appl. Phys. **102**, 074905 (2007).
[18]C. A. McPhee and K. G. Arthur, Edinburgh Petroleum Services Limited, UK.
[19]R. F. Cracknell, D. Nicholson, and N. Quirke, Phys. Rev. Lett. **74**, 2463 (1995).
[20]D. M. Ford and E. D. Glandt, J. Phys. Chem. **99**, 11543 (1995).
[21]D. M. Ford and G. S. Heffelfinger, Mol. Phys. **94**, 673 (1998).
[22]S. Furukawa, K. Hayashi, and T. Nitta, J. Chem. Eng. Jpn. **30**, 1107 (1997).
[23]G. S. Heffelfinger and F. V. Swol, J. Chem. Phys. **100**, 7548 (1994).
[24]G. S. Heffelfinger and D. M. Ford, Mol. Phys. **94**, 659 (1998).
[25]S. Kjelstrup and B. Hafskjold, Ind. Eng. Chem. Res. **35**, 4203 (1996).
[26]M. Lupkowski and F. V. Swol, J. Chem. Phys. **95**, 1995 (1991).
[27]J. M. D. MacElroy, J. Chem. Phys. **101**, 5274 (1994).
[28]E. J. Maginn, A. T. Bell, and D. N. Theodorou, J. Phys. Chem. **97**, 4173 (1993).
[29]D. Nicholson, R. F. Cracknell, and N. Quirke, Langmuir **12**, 4050 (1996).
[30]P. I. Pohl and G. S. Heffelfinger, J. Membr. Sci. **155**, 1 (1999).
[31]M. Sun and C. Ebner, Phys. Rev. A **46**, 4813 (1992).
[32]S. Sunderrajan, C. K. Hall, and B. D. Freeman, J. Chem. Phys. **105**, 1621 (1996).
[33]A. P. Thompson, D. M. Ford, and G. S. Heffelfinger, J. Chem. Phys. **109**, 6406 (1998).
[34]L. Xu, M. G. Sedigh, M. Sahimi, and T. T. Tsotsis, Phys. Rev. Lett. **80**, 3511 (1998).
[35]L. Xu, T. T. Tsotsis, and M. Sahimi, J. Chem. Phys. **111**, 3252 (1999).
[36]L. Xu, T. T. Tsotsis, and M. Sahimi, Phys. Rev. E **62**, 6942 (2000).
[37]L. Xu, M. G. Sedigh, T. T. Tsotsis, and M. Sahimi, J. Chem. Phys. **112**, 910 (2000).
[38]M. Firouzi, T. T. Tsotsis, and M. Sahimi, J. Chem. Phys. **119**, 6810 (2003).
[39]M. Firouzi, Kh. Molaai Nezhad, T. T. Tsotsis, and M. Sahimi, J. Chem. Phys. **120**, 8172 (2004).
[40]M. Firouzi, M., Sahimi, and T. T. Tsotsis, Phys. Rev. E **73**, 036312 (2006).
[41]M. Firouzi, T. T. Tsotsis, and M. Sahimi, Chem. Eng. Sci. **62**, 2777 (2007).
[42]M. Firouzi and J. Wilcox, Microporous Mesoporous Mater. **158**, 195 (2012).
[43]See supplementary material at http://dx.doi.org/10.1063/1.4790658 for the computed pore size distribution (PSD), the time-averaged velocity profiles, the velocity autocorrelation function, and the self-diffusivities.
[44]J. K. Johnson, J. A. Zollweg, and K. E. Gubbins, Mol. Phys. **78**, 591 (1993).
[45]D. M. Ruthven, *Principles of Adsorption & Adsorption Processes* (Wiley, 1984).
[46]M. P. Allen and D. J. Tildesley, *Computer Simulation of Liquids* (Oxford University Press, Oxford, 1987).
[47]D. Cao and J. Wu, Langmuir **20**, 3759 (2004).
[48]M. Khademi and M. Sahimi, J. Chem. Phys. **135**, 204509 (2011).
[49]Y. Bae, O. K. Farha, J. T. Hupp, and R. Q. Snurr, J. Mater. Chem. **19**, 2131 (2009).
[50]Y. Liu and J. Wilcox, Environ. Sci. Technol. **46**, 1940 (2012).
[51]M. Sahimi and T. T. Tsotsis, Physica B **338**, 291 (2003).
[52]V. P. Sokhan, D. Nicholson, and N. Quirke, J. Chem. Phys. **117**, 8531 (2002).
[53]A. Thomas and A. J. H. McGaughey, Nano Lett. **8**, 2788 (2008).
[54]A. Rahman and F. H. Stillinger, J. Chem. Phys. **55**, 3336 (1971).